TU Delft

Delft University of Technology

Document Version
Final published version

Licence
Dutch Copyright Act (Article 25fa)

Citation (APA)
Shen, Q., van Rooij, F., Zhang, Z., Hao, W., Dugulan, A. I., van Dijk, N., Brück, E., & Li, L. (2026). Tunable magnetoelastic transition and enhanced magnetocaloric response in $Hf_{0.82}Ta_{0.18}Fe_2$ Laves phase alloys by Fe(6h)-site manipulation. *Journal of Materials Science and Technology*, *254*, 196-205. https://doi.org/10.1016/j.jmst.2025.08.015

Important note
To cite this publication, please use the final published version (if applicable).
Please check the document version above.

Copyright
In case the licence states “Dutch Copyright Act (Article 25fa)”, this publication was made available Green Open Access via the TU Delft Institutional Repository pursuant to Dutch Copyright Act (Article 25fa, the Taverne amendment). This provision does not affect copyright ownership.
Unless copyright is transferred by contract or statute, it remains with the copyright holder.

Sharing and reuse
Other than for strictly personal use, it is not permitted to download, forward or distribute the text or part of it, without the consent of the author(s) and/or copyright holder(s), unless the work is under an open content license such as Creative Commons.

Takedown policy
Please contact us and provide details if you believe this document breaches copyrights.
We will remove access to the work immediately and investigate your claim.

This work is downloaded from Delft University of Technology.

Journal of Materials Science & Technology 254 (2026) 196–205

Contents lists available at ScienceDirect

Journal of Materials Science & Technology

journal homepage: www.elsevier.com/locate/jmst

Research Article

Tunable magnetoelastic transition and enhanced magnetocaloric response in $Hf_{0.82}Ta_{0.18}Fe_2$ Laves phase alloys by Fe(6*h*)-site manipulation

Qi Shen[a,b], Floris van Rooij[b], Zeyu Zhang[a], Weixiang Hao[a], Achim Iulian Dugulan[b], Niels van Dijk[b], Ekkes Brück[b], Lingwei Li[a,*]

[a] Key Laboratory of Novel Materials for Sensor of Zhejiang Province, Hangzhou Dianzi University, Hangzhou 310012, China
[b] Fundamental Aspects of Materials and Energy, Faculty of Applied Sciences, Delft University of Technology, Mekelweg 15, 2629 JB Delft, The Netherlands

ARTICLE INFO

Article history:
Received 16 April 2025
Revised 24 June 2025
Accepted 7 August 2025
Available online 28 August 2025

Keywords:
Magnetoelastic transition
Magnetocaloric effect
Neutron powder diffraction
Mössbauer spectroscopy

ABSTRACT

We herein provide a combined experimental investigation and theoretical calculations on the impact of Mn doping and Fe off-stoichiometry on the magnetoelastic transition and the magnetocaloric properties of Laves phase $Hf_{0.82}Ta_{0.18}Fe_2$ alloys. Mn substitution led to an increase in unit-cell volume while Fe vacancies induced lattice contraction. By adjusting the Mn and Fe content, we achieved a table-like magnetocaloric response with a magnetic entropy change of 1.7–2.2 J/(kg K) at a magnetic field change of 2 T over a wide temperature range from 190 to 260 K. Mössbauer spectroscopy, neutron powder diffraction and density functional theory calculations all reveal that both Mn atoms and Fe vacancies preferentially occupy the 6*h* crystallographic site of the lattice structure with space group $P6_3/mmc$, and that the shortest intralayer Fe-6*h* interatomic distance governs the magnetoelastic transition in (Hf, Ta)Fe_2 Laves phases. The tunable magnetic transition is ascribed to the slight change of the electronic state of the Fe-6*h* site and limited hybridization between Mn and Fe atoms. These findings offer new insight into the site-specific control for optimizing the magnetocaloric properties of Fe-based Laves phase alloys and inspire the design of other promising magnetocaloric materials with magnetoelastic transitions.

© 2026 Published by Elsevier Ltd on behalf of The editorial office of Journal of Materials Science & Technology.

1. Introduction

Magnetic refrigeration based on the magnetocaloric effect (MCE) is emerging as a sustainable alternative to conventional cooling technologies. Magnetocaloric materials are characterized by either an isothermal magnetic entropy change (ΔS_M) or an adiabatic temperature change (ΔT_{ad}) when subjected to a change in external magnetic field [1–6]. Over the past three decades, research interest in MCE has surged, particularly after the discovery of a giant MCE (13 J/(kg K) in a magnetic field change of 2 T) in $Gd_5Si_2Ge_2$, which has a Curie temperature (T_C) of 270 K [7]. Unlike materials with a second-order magnetic transition (SOMT), such as Gd, which shows a moderate entropy change, materials with a first-order magnetic transition (FOMT), such as FeRh [8], $La(Fe,Si)_{13}$ [9,10], $(Mn,Fe)_2(P,Si)$ [1,11], $(Mn,Cr)_2Sb$ [12], and (Hf,Ta)Fe_2 [13] display larger (absolute) values of ΔS_M or ΔT_{ad} due to their strong coupling of magnetic and lattice degrees of freedom. Among the FOMT materials, those exhibiting "order-order" magnetic transitions, which involve magnetic transitions without altering the crystal symmetry, such as the antiferromagnetic-to-ferromagnetic transition in FeRh, the antiferromagnetic-to-ferrimagnetic transition in $(Mn,Cr)_2Sb$, or the ferromagnetic-to-antiferromagnetic (FM-AFM) transition in (Hf,Ta)Fe_2 upon heating, have unique characteristics. These transitions, which couple spin and lattice degrees of freedom, offer advantages such as a low thermal hysteresis [12,14], a high field sensitivity [8,14], and a good reversibility in moderate magnetic fields [13,15], making them suitable for high-performance magnetocaloric applications.

The (Hf,Ta)Fe_2 Laves phase alloys have attracted attention as promising magnetocaloric material due to their pronounced FM-AFM transition, low hysteresis, tunable transition temperature (T_t), and large adiabatic temperature [6,13,16–18]. Laves phase, a topological stacked intermetallic compound, has wide applications in areas such as hydrogen storage [19,20], superconductivity [21,22], and magnetostriction [23,24]. Besides, a large MCE near room temperature has been reported in (Hf,Ta)Fe_2 alloys, which crystallize in

* Corresponding author.
E-mail address: lingwei@hdu.edu.cn (L. Li).

https://doi.org/10.1016/j.jmst.2025.08.015
1005-0302/© 2026 Published by Elsevier Ltd on behalf of The editorial office of Journal of Materials Science & Technology.

Table 1
Chemical composition (in at. %) determined by EDS for the Mn-doped and Fe-deficient alloys.

	Fe	Mn	Ta	Hf
Mn0	66.61(0.17)	0	5.77(0.16)	27.61(0.19)
Mn2	66.66(0.17)	0.24(0.04)	5.05(0.16)	28.05(0.19)
Mn4	65.35(0.17)	0.52(0.07)	5.98(0.16)	28.14(0.19)
Mn6	65.79(0.34)	0.82(0.09)	6.61(0.16)	26.78(0.29)
Fe1.94	66.41(0.17)	–	5.53(0.05)	28.06(0.12)
Fe1.96	66.36(0.17)	–	5.74(0.07)	27.90(0.12)
Fe1.98	66.20(0.17)	–	6.03(0.07)	27.77(0.12)

the hexagonal $MgZn_2$ crystal structure with space group $P6_3/mmc$ [13,25,26]. For example, $Hf_{0.84}Ta_{0.16}Fe_2$ exhibits a ΔT_{ad} value up to 3.4 K obtained at 253 K under a magnetic field change of 1.5 T [13]. The magnetocaloric properties of (Hf,Ta)Fe_2 arise from its unique AFM configuration, where Fe atoms occupy two crystallographic sites, 2*a* and 6*h* , within the hexagonal *C*14-type structure [27]. The magnetic moment of Fe atoms at the 6*h* site align ferromagnetically within the *a*–*b* plane, while those of the 2*a* site are magnetically frustrated (the time-average magnetic moment disappears) below T_t, leading to a lattice contraction of about 1 % [16,28,29]. Element doping and off-stoichiometry are common strategies to modify the thermal and magnetic properties in magnetocaloric materials. $Hf_{0.85}Ta_{0.13}Fe_{2+x}$ alloys form a single *C*14-symmetry Laves phase with a modified negative thermal effect for < 0.43 [30,31], while the magnetic transitions change from a FOMT into a SOMT for > 0.1. Conversely, a sub-stoichiometric Fe content sharpens the AFM-FM transition [32]. Doping with elements such as C and Co also affects the magnetocaloric properties: carbon doping enhances the magnetoelastic coupling and increases $|\Delta S_M|$ from 1.8 J/(kg K) for $Hf_{0.85}Ta_{0.15}Fe_2$ to 4.0 J/(kg K) for $Hf_{0.85}Ta_{0.15}Fe_2C_{0.01}$ in a magnetic field change of 2 T with a low thermal expansion coefficient of 2.4 ppm/K [33]; Co doping reduces T_t, while maintaining a significant magnetic entropy change [34]. Even though the potential of MCE systems with an order-order transition to broaden magnetocaloric applications, systematic studies of such materials remain limited compared to MCE systems with an order-disorder transition. Moreover, the role of off-stoichiometric Fe atoms and doping elements in the magnetoelastic transition remains unclear.

In this paper, we explore the effects of Mn doping and Fe off-stoichiometry on the magnetic properties of (Hf,Ta)Fe_2 alloys. We achieve a table-like magnetic entropy change between 1.7 and 2.2 J/(kg K) at 2 T across a broad temperature range (190–260 K) by tuning Mn and Fe concentrations. Using density functional theory (DFT) calculations, Mössbauer spectroscopy, and neutron powder diffraction (NPD) techniques, we investigate the occupancy of Mn atoms and Fe vacancies and their influence on crystal structure, magnetoelastic transition, and the magnetocaloric response.

2. Experimental methods

Polycrystalline $Fe_{2-x}Mn_xHf_{0.82}Ta_{0.18}$ ($x = 0$, 0.02, 0.04, 0.06) and $Fe_yHf_{0.82}Ta_{0.18}$ ($y = 1.94$, 1.96, and 1.98) alloys were prepared from high-purity elements (Fe 99.98 %, Mn 99.9 %, Hf 99.7 %, Ta 99.7 %) by arc melting. The alloys were prepared by arc-melting approximately 5 g of material under an argon atmosphere. To ensure homogeneity, each button-shaped sample was melted four to five times. The samples were flipped after each melt. For ease of reference, the $x = 0$, 0.02, 0.04, and 0.06 samples are denoted as Mn0, Mn2, Mn4, and Mn6 alloys, and the $y = 1.94$, 1.96, and 1.98 samples as Fe1.94, Fe1.96, and Fe1.98 alloys, respectively. The compositions of the resulting alloys given in Table 1 were determined by Energy Dispersive X-ray Spectroscopy (EDS). Since previous studies on $Fe_2Hf_{0.83}Ta_{0.17}$ [14] showed that the heat treatment had minimal effect on magnetic properties, no additional annealing was performed on these samples.

Phase identification and crystal structure analysis were conducted using X-ray diffraction (XRD) on a Panalytical X-Pert PRO diffractometer with Cu-Kα radiation. Rietveld refinement was performed using the FullProf software suite [35]. The magnetic properties of the samples were measured over a temperature range of 4–370 K using a superconducting quantum interference device (SQUID) magnetometer (MPMS–XL) equipped with a reciprocating sample option. The ferromagnetic transition temperature T_t was determined from the minimum in the derivative of the magnetization–temperature (*M*–*T*) curves upon cooling at an applied magnetic field of 1 T Magnetic entropy changes were calculated from *M*–*T* curves measured at various magnetic field strengths, using the Maxwell relation. Scanning electron microscopy (SEM) was used to analyze the sample microstructure and confirm elemental distribution within each alloy. The SEM analysis was performed on an FEI Quanta FEG 450 microscope equipped with an energy-dispersive X-ray spectroscopy (EDS) detector. The chemical compositions obtained from EDS analysis are presented in Table 1 for reference. Transmission ^{57}Fe Mössbauer spectra were collected across various temperatures using a constant-acceleration or sinusoidal velocity spectrometer with a ^{57}Co(Rh) source. Velocity calibration was performed at room temperature using an α-Fe foil, and the source and samples were maintained at the same temperature during cryogenic measurements. Mössbauer spectra were analyzed using the MossWinn 4.0 program [36], with a particular focus on the identification of hyperfine interactions related to the 2*a* and 6*h* sites. NPD data at different temperatures were collected at a wavelength of 1.6672 Å using the NPD apparatus PEARL [37] at the research reactor of Delft University of Technology. The crystal structures and the atomic occupancies were refined using the Rietveld refinement method implemented in the Fullprof software package [38,39].

3. DFT calculations

First-principles calculations based on DFT calculations were conducted to investigate the electronic and magnetic structures of Fe-Mn-Hf-Ta alloys. To enable a comparison between experimental and simulation results, we utilized chemical compositions closely resembling the nominal compositions $Hf_{0.82}Ta_{0.18}Fe_2$, including $Hf_{0.80}Ta_{0.20}Fe_2$ as the parent alloy, $Hf_{0.80}Ta_{0.20}Fe_{1.95}Mn_{0.05}$ and $Hf_{0.80}Ta_{0.20}Fe_{1.75}Mn_{0.25}$ as the Mn-doped alloy, and $Hf_{0.80}Ta_{0.20}Fe_{1.95}$ and $Hf_{0.80}Ta_{0.20}Fe_{1.75}$ as the Fe-deficient alloy. DFT calculations were performed using the Vienna Ab Initio Simulation Package (VASP) [40,41] with plane-wave basis sets. An energy cutoff of 520 eV was applied, and pseudopotentials were defined using the projected augmented wave (PAW) method with valence configurations $3d^6\ 4s^2$ for Fe, $5d^2\ 6s^2$ for Hf, $5d^3\ 6s^2$ for Ta, and $3d^5\ 4s^2$ for Mn [42,43]. Exchange-correlation interactions were modeled using the Perdew-Burke-Ernzerhof (PBE) functional within the generalized gradient approximation (GGA), and a Monkhorst-Pack *k*-point grid of $2 \times 2 \times 4$ based on a 120-atoms supercell was employed for both structural optimization and electronic properties calculations [44]. Convergence criteria for the Hellmann-Feynman forces were set at <0.01 eV/Å, with an electronic loop convergence threshold of 10^{-5} eV. The formation energy E_f was calculated as follows: $E_f = E_{compound} - \sum_i x_i E_i$, where $E_{compound}$ represents the optimized total energy of the compound, and x_i and E_i are the stoichiometric coefficients and ground-state energies of Fe, Hf, Ta, and Mn atoms in their reference states, respectively. A lower E_f indicates higher stability of the alloy, which can be used to obtain the preferred atomic site occupations.

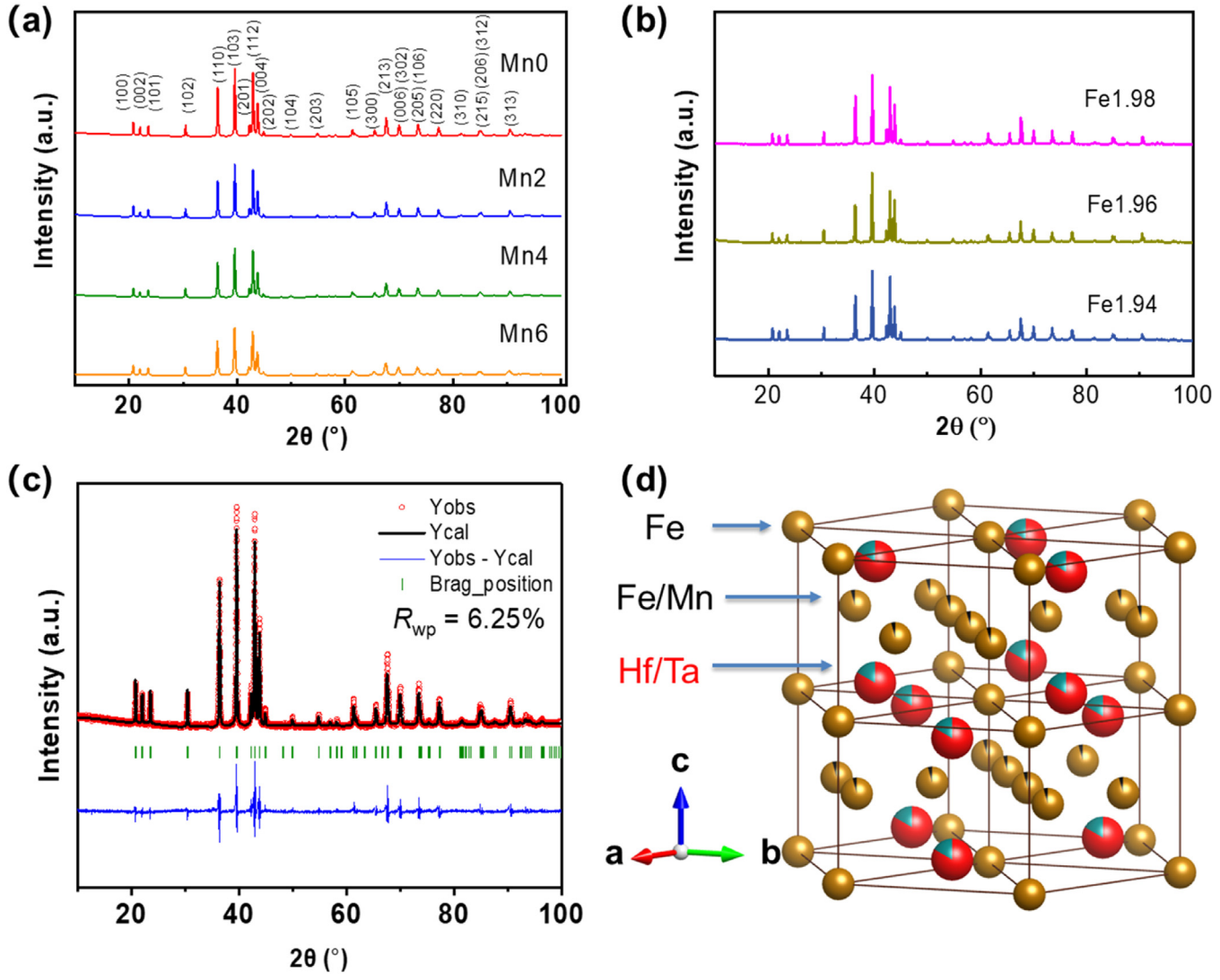

Fig. 1. XRD patterns for (a) Mn0, Mn2, Mn4, and Mn6 and for (b) Fe1.94, Fe1.96, and Fe1.98 alloys. (c) Rietveld-refined XRD pattern of Mn0. (d) Crystal structure of $MgZn_2$-type (Hf,Ta)Fe_2 alloys.

4. Results and discussion

The crystal structure of $Hf_{0.82}Ta_{0.18}Fe_{2-x}Mn_x$ (x = 0, 0.02, 0.04, and 0.06) and $Hf_{0.82}Ta_{0.18}Fe_y$ (y = 1.94, 1.96, and 1.98) alloys were analyzed by XRD patterns as shown in Fig. 1. All alloys crystallize in a single-phase hexagonal structure with the $MgZn_2$-type $C14$ symmetry. The refined XRD patterns, with an example of Mn0 in Fig. 1(b), confirm phase purity across the alloy series. Fig. 1(c) depicts the hexagonal structure of (Hf,Ta)Fe_2-based alloys, where Fe occupies two sites, 2a and 6h sites, and Ta/Hf occupies the 4f site. The SEM images, as shown in Fig. 2, further prove the homogeneity of $Fe_{2-x}Mn_xHf_{0.82}Ta_{0.18}$ and $Fe_{2-y}Hf_{0.80}Ta_{0.20}$ alloys. Mn substitution generally expands the unit-cell volume V, as shown in Fig. 3(a), due to Mn's larger atomic radius (1.27 Å) compared to Fe (1.26 Å) [45]. Both the lattice parameters a and the V increase continuously for increasing Mn content. For the Mn2 alloy, a minor drop in the c-axis is observed. For the Fe-deficient alloys, as shown in Fig. 3(b), a clear contraction in the unit-cell volume is observed for increasing Fe content, reflecting a lattice response to vacancies. The decrease in unit-cell volume with increasing Fe content aligns with previous studies of Fe-based Laves phases such as $Hf_{0.80}Nb_{0.20}Fe_{2-x}$ [46] and $Hf_{0.83}Ta_{0.17}Fe_{2+x}$ [32], where Fe atoms partially substitute into Hf/Ta 4f sites, promoting volume adjustments [30]. The chemical compositions obtained from EDS and listed in Table 1 align closely with the nominal compositions, except for minor deviations in the Ta content for the Mn2 alloy. The measured Ta/Hf ratios for the samples (Mn0: 0.219, Mn2: 0.180, Mn4: 0.213, Mn6: 0.247) show an initial decrease followed by an increase with increasing Mn content. Although Mn loss can occur during arc melting, these measurements confirmed the proportional increase in Mn content with nominal doping.

Fig. 4 displays the M–T and M–H curves of $Hf_{0.82}Ta_{0.18}Fe_{2-x}Mn_x$ and $Hf_{0.82}Ta_{0.18}Fe_y$ alloys. The M–T curves in Fig. 4(a, b), measured under an applied field of 0.01 T and 1 T, respectively, exhibit a pronounced decrease in magnetization with increasing temperature, indicative of the FM-AFM transition. The FM-AFM transition temperature T_t decreases with increasing Mn content, except for the Mn2 alloy, which shows an anomalously high T_t of 245 K under a magnetic field of 1 T, potentially due to a minor deviation in the Ta/Hf ratio, as observed in the EDS analysis. The T_t values for Mn0, Mn4, and Mn6 are 215, 183, and 154 K, respectively. A reduced Ta concentration is known to shift the transition to higher temperature and promote a tendency toward a second-order magnetoelastic transition, as reported in previous studies [13]. However, our

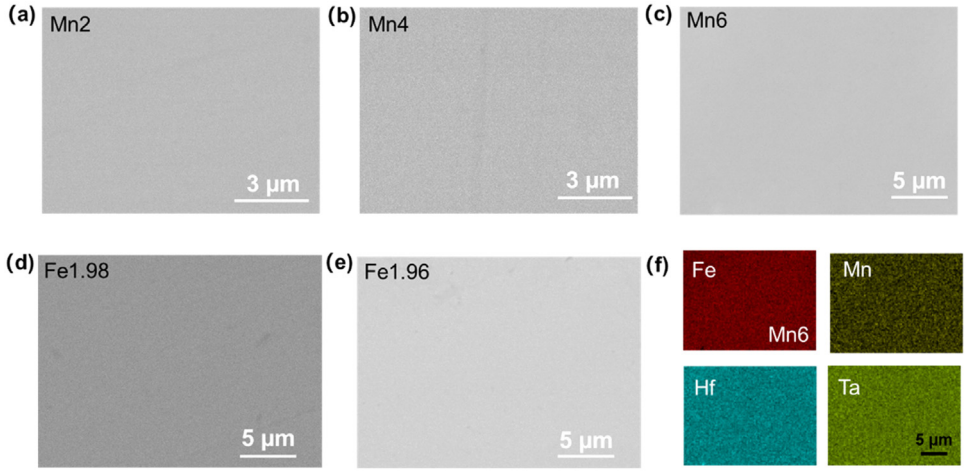

Fig. 2. (a–e) SEM images of the Mn2, Mn4, Mn6, Fe1.98, and Fe1.96 alloys. (f) Elemental mapping of the Mn6 alloy showing uniform distribution of Fe, Mn, Hf, and Ta atoms.

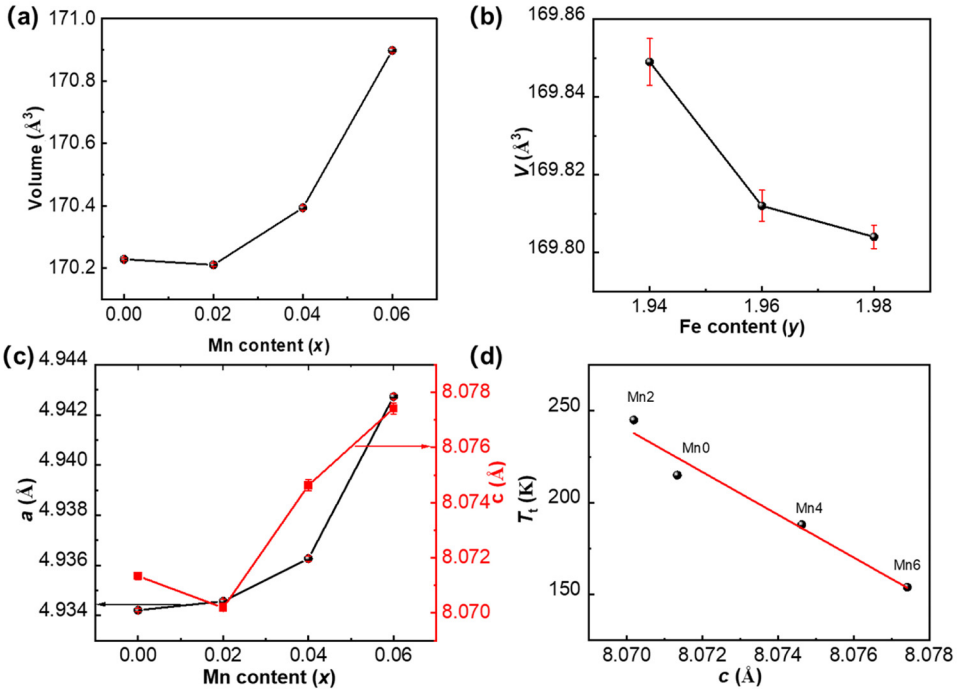

Fig. 3. Unit-cell volume V for (a) Mn0, Mn2, Mn4, and Mn6 alloys and for (b) Fe1.94, Fe1.96, and Fe1.98 alloys. (c) lattice parameter a and c for the Mn0, Mn2, Mn4 and Mn6 alloys as a function Mn content. (d) T_t as a function of lattice parameter c.

results show that the Mn2 alloy still exhibits a sharp FOMT (discussed later) with the higher T_t. This behavior is attributed to the combined effect of slight Mn doping and the subtle change in Ta/Hf ratio, suggesting an intricate interplay between compositional tuning and magnetic transition characteristics.

Despite the anomaly in Mn2, a near-linear relationship between T_t and the lattice parameter c is observed in Fig. 3(d), underscoring the sensitivity of the transition temperature to structural changes induced by Mn doping. For the Mn6 alloy, a magnetization bump is observed in the M–T curve in a magnetic field of 0.01 T, likely resulting from an inhomogeneous distribution of Mn atoms, similar to the two-step magnetic transition previously reported in the $Hf_{0.80}Nb_{0.20}Fe_{1.95}$ alloy due to Fe vacancies [46]. In Fig. 4(c), the M–H curves at 5 K reveal that Mn-doped alloys generally exhibit comparable saturation magnetization M_s values, approximately 2.4–2.6 μ_B/f.u., with the Fe1.96 alloy showing a slightly lower magnetization in 1 T, likely due to induced magnetic anisotropy by Fe vacancies [46]. Thermal hysteresis of 2 K is observed near T_t in the Mn2 alloy, while Mn0 and Mn4 show slightly larger hysteresis values of 3–5 K at the onset of the FM-AFM transition. In contrast, the Fe-deficient alloys exhibit near-zero thermal hysteresis as shown in Fig. 4(d), with T_t decreasing from 263 K in Fe1.94 to 253 K in Fe1.98. Among these, the Fe1.98 alloy displays the sharpest magnetization curve, consistent with previous reports that a slightly Fe-deficient, as-cast alloy tends to exhibit sharper FM-AFM transition [32].

To quantify the magnetic entropy change, a series of M–T curves upon heating was collected for $Hf_{0.82}Ta_{0.18}Fe_{2-x}Mn_x$ and $Hf_{0.82}Ta_{0.18}Fe_y$ at various magnetic fields, as shown in Figs. 5(a–c) and S1 in Supplementary materials. The highest $|\Delta S_M|$ values are observed in the Mn0 and Mn2 alloys, reaching 2.0–2.1 J/(kg K), which is comparable to other (Hf,Ta)Fe_2 alloys with a FOMT, such as 2.4 J/(kg K) in $Hf_{0.86}Ta_{0.14}Fe_2$ [25] and 3.0 J/(kg K) in $Ta_{0.15}Fe_2Hf_{0.85}$ [13]. The Mn4 and Fe1.96 alloys exhibit $|\Delta S_M|$ val-

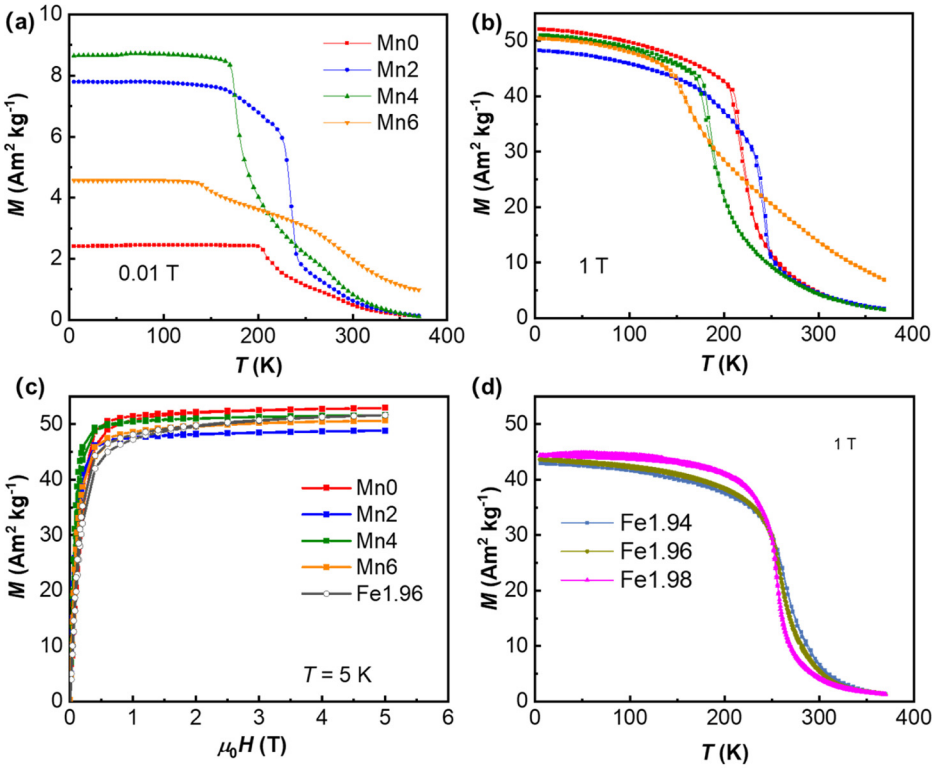

Fig. 4. *M–T* curves of Mn0, Mn2, Mn4, and Mn6 alloys (a) in a magnetic field of 0.01 T and (b) in a magnetic field of 1 T (c) *M–H* curves of Mn0, Mn2, Mn4, Mn6, and Fe1.96 alloys at 5 K. (d) *M–T* curves of Fe1.94, Fe1.96, and Fe1.98 alloys in a magnetic field of 1 T.

ues around 1.6–1.7 J/(kg K). The Mn6 alloy, however, shows a reduced $|\Delta S_M|$ of 0.7 J/ (kg K), likely due to broader *M–T* curves. A significant feature of these alloys is a "table-like" entropy change (a plateau in the $|\Delta S_M|$ curve) [47] with $|\Delta S_M|$ exceeding 1.7 J/(kg K) over a wide temperature range of approximately 70 K. Although ferrimagnetic Mn_2Hf crystalizes in the same *C*14 structure, the solubility limit of Mn substitution in (Hf,Ta)Fe_2 system is $x = 0.06$. Interestingly, the $Hf_{0.80}Ta_{0.20}Fe_{1.97}Co_{0.03}$ alloy shows a coexistence of FM and AFM phases [48], indicating that Co has an even lower solubility limit in the (Hf,Ta)Fe_2 system than Mn. For Co substitutions in $Hf_{0.9}Ta_{0.1}Fe_2$, the structure transforms from the hexagonal *C*14 structure to the cubic *C*15 structure with increasing Co, adopting the cubic structure of Co_2Hf [49]. The Arrott plot for the Mn2 alloy in Fig. 5(e) exhibits *S*-shaped curves, suggesting a FOMT, further supported by the thermal hysteresis observed in the *M–T* curve. Other alloys, such as Mn0, Mn4, Fe1.96, and Fe1.98 alloys, show weaker *S*-shape profiles, as present in supplementary Fig. S2, indicating a less pronounced FOMT compared to Mn2. The minor amounts of Mn appear to play an important role in the frustration effect within (Hf,Ta)Fe_2 alloys, which is highly sensitive to electronic structure modifications by elemental substitutions [50]. Notably, even a minor amount of Co in $Fe_{1.97}Co_{0.03}Hf_{0.80}Ta_{0.20}$ causes the disappearance of the AFM-FM transition [48]. The dependence of T_t on the applied magnetic field with a slope m ($T_t/\mu_0 H$) of 8.0, 8.1, 9.0 K/T for Mn0, Mn2, and Mn4 alloy, respectively, aligns well with previous reported values, such as 8.6 K/T for $Fe_2Hf_{0.83}Ta_{0.17}$ [14] and 7.7 K/T for $Hf_{0.85}Ta_{0.15}Fe_2$ [51]. Interestingly, the slope m for Mn4 matches that of $Fe_{48}Rh_{52}$, which also exhibits an order-order magnetic transition [52]. Mn substitution thus provides a means to adjust the slope m, where a large m enables a more complete phase transition in a limited applied magnetic field [2,53].

To explore the impact of Mn doping on the magnetoelastic transition in $Hf_{0.82}Ta_{0.18}Fe_{2-x}Mn_x$ alloys, Mössbauer spectroscopy and NPD were conducted on the Mn0, Mn2, and Mn4 alloys. The Mössbauer spectra for the Mn0 and Mn2 alloys, shown in Fig. 6, were analyzed based on the crystal structure, where Fe occupies two distinct sites: 2*a* and 6*h* sites, with an atom ratio of 1:3 [14,54]. The spectrum at 400 K confirms the PM state at high temperatures. At room temperature, spectra for both the Mn0 and Mn2 alloys contain two magnetic sub-spectra, corresponding to the Fe(6*h*) and Fe(2*a*) sites, indicative of the AFM phase. The hyperfine field B_{hf} of Fe(6*h*) in the AFM phase is about one-third of its value in the FM phase, while the B_{hf} of Fe(2*a*) is zero due to the frustration effect [28]. At 4.2 K, the spectra exhibit four sextets with equal area contributions, assigned to Fe atoms at the 2*a* site and to the three 6*h* sites in the FM phase, reflecting different spin reorientations relative to the electronic field gradient's principal axis [14,55]. The hyperfine parameters from Mössbauer analysis, summarized in Table 2, show consistent isomer shifts for the Mn0 and Mn2 alloys at the same temperature. However, the quadrupole splitting for the 6*h* site differs between the Mn0 and Mn2 alloys at 4 K, suggesting that Mn doping influences the valence and electronic state of the Fe atoms. The stronger magnetoelastic coupling observed in the Mn2 alloy can be attributed to the slightly altered chemical environment at the 6*h* Fe site in $Hf_{0.82}Ta_{0.18}Fe_2$, as supported by Mössbauer analysis. The calculated magnetic moments for the Mn0 and Mn2 alloys, derived from a proportionality factor of 14.2 T/μ_B proposed by Eriksson and Svane [56] are 2.42 μ_B and 2.43 μ_B, respectively. The lower hyperfine fields for Fe at the 2*a* and 6*h* sites of the Mn2 alloy compared to the Mn0 alloy are consistent with its lower saturation magnetization.

NPD analysis was conducted to refine the crystal and magnetic structures of Mn0, Mn2, and Mn4 at various temperatures. The comparison of NPD and XRD data at 300 K is given in Table S1. The unit-cell volumes of the Mn0 and Mn2 alloys are comparable, and both are smaller than that of the Mn4 alloy, which is consistent with the trend observed in the XRD results. Fig. 7 displays the NPD pattern of Mn0 at 400 K, representing the PM phase, and

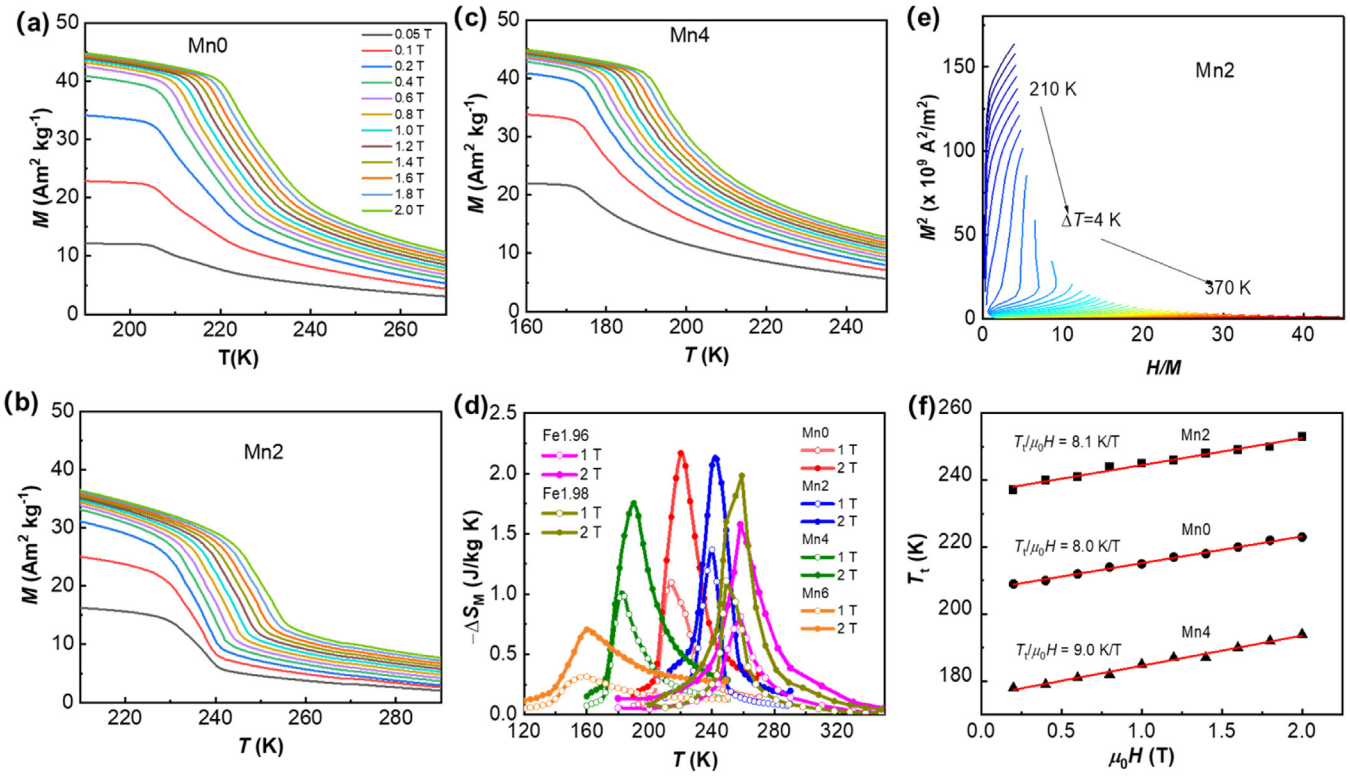

Fig. 5. *M–T* curves upon heating in different applied magnetic fields for the (a) Mn0 alloy, (b) Mn2 alloy, and (c) Mn4 alloy. (d) $|\Delta S_M|$ calculated from the heating curves for all alloys. (e) Arrott-plot of the Mn2 alloy. (f) Magnetic field dependence of the transition temperature ($T_t/\mu_0 H$) for the Mn0, Mn2, and Mn4 alloys.

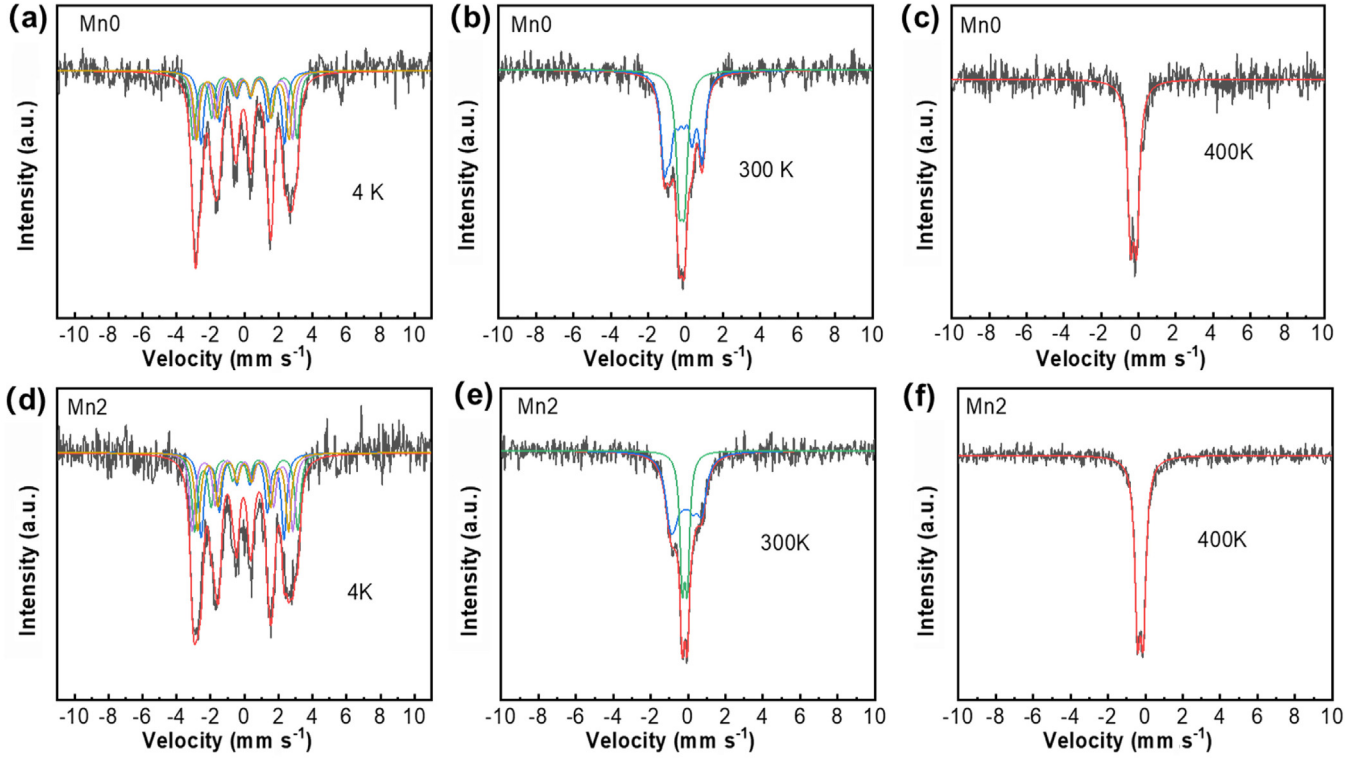

Fig. 6. Mössbauer spectra for Mn0 alloy at (a) 4 K, (b) 300 K, and (c) 400 K. Mössbauer spectra for the Mn2 alloy at (d) 4 K, (e) 300 K, and (f) 400 K.

Table 2
Experimental uncertainties: isomer shift: I.S. ±0.03 mm s^{-1}; quadrupole splitting Q.S.: ±0.03 mm s^{-1}; line width Γ: ±0.05 mm s^{-1}; hyperfine field: ±0.2 T; spectral contribution: ±3 %.

Sample	Tempera-ture (K)	IS (mm s^{-1})	QS (mm s^{-1})	Hyperfine field (T)	Γ (mm s^{-1})	Phase
Mn0	400	−0.25	0.33	–	0.37	100 % PM
	300	−0.20	0.28	–	0.41	38.64 % 2*a*
		−0.19	0.12	6.30	0.43	61.36 % 6*h*
	4	−0.08	−0.06	15.24	0.37	25.03 % 2*a*
		−0.07	0.19	18.97	0.39	24.99 % 6*h*
		−0.06	0.06	17.74	0.39	24.99 % 6*h*
		−0.07	−0.07	16.87	0.39	24.99 % 6*h*
Mn2	400	−0.27	0.31	–	0.36	100 % PM
	300	−0.18	0.27	–	0.30	36.57 % 2*a*
		−0.18	0.11	5.27	0.62	64.43 % 6*h*
	4	−0.09	−0.05	15.15	0.36	25.16 % 2*a*
		−0.06	0.30	18.87	0.39	24.95 % 6*h*
		−0.06	−0.11	18.38	0.39	24.95 % 6*h*
		−0.05	−0.07	16.61	0.39	24.95 % 6*h*

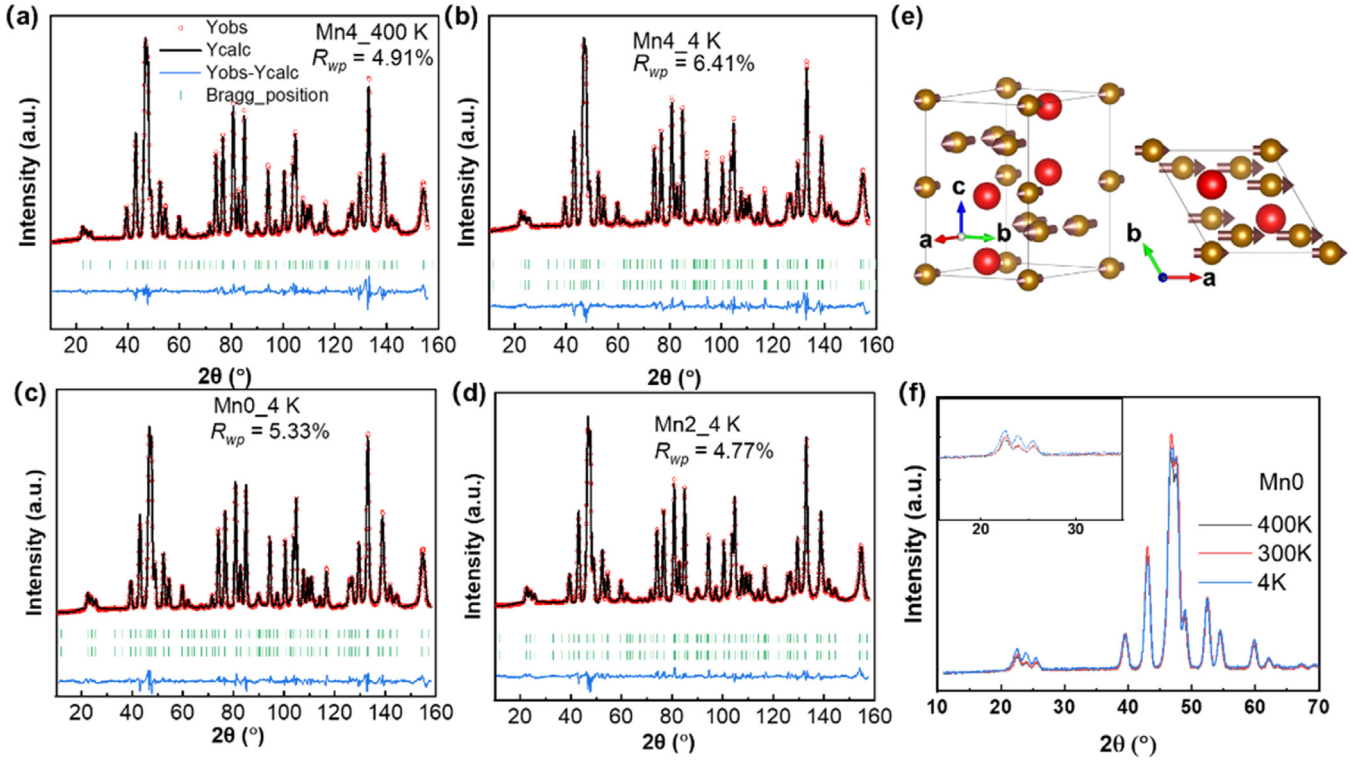

Fig. 7. NPD patterns for the Mn4 alloy (a) at 400 K showing nuclear Bragg peaks (PM phase) and (b) at 4 K with magnetic contributions (FM phase). The top row of marked Bragg peak positions is from the nuclear contribution. The second row in (b) corresponds to the magnetic contribution. NPD patterns at 4 K for the (c) Mn0 and (d) Mn2 alloys. (e) Refined magnetic moment configuration of the FM phase. (f) Enlarged range of NPD patterns for the Mn0 alloy at 400, 300, and 4 K, illustrating the evolution of magnetic peak intensity.

of Mn0, Mn2, and Mn4 at 4 K, indicating the FM phase. At 400 K, the diffraction pattern characteristic of nuclear Bragg scattering fits well to the $MgZn_2$-type phase with $P6_3/mmc$ symmetry, thereby confirming the hexagonal structure of the PM phase. Complementing XRD, NPD offers enhanced sensitivity to light or neighboring elements, and the substantial distance in coherent scattering length between Fe (9.45 fm) and Mn (−3.73 fm) enables precise determination of Mn's site occupancy. Rietveld refinements on the low-temperature (4 K) NPD data indicate that Mn predominantly occupies the 6*h* site, supported by the lowest χ^2 value (18.4) obtained when Mn is modeled at the 6*h* position, compared to 19.3 and 19.7 for Mn at the 2*a* and 4*f* sites, respectively [57]. Analysis of the magnetic reflections, especially at the (100), (101), and (002) peaks, confirms that the magnetic unit cell is equal in size to the nuclear unit cell and that the magnetic moments are oriented within the *a*–*b* plane. At 300 K, weak AFM contributions are detected, with only a slight magnetic intensity at the (100) peak, as shown in Fig. 7(f). The refined parameters listed in Table 3, confirm that the Fe moments at the 2*a* site are smaller than those at the 6*h* site. The total magnetic moments calculated from NPD for the Mn0, Mn2, and Mn4 alloys are 2.88, 2.48, and 2.58 μ_B/f.u., respectively, consistent with values obtained from SQUID and Mössbauer analyses. The *c*/*a* ratio initially increases with temperatures up to 300 K, then decreases as the temperature rises further. Additionally, the NPD patterns for Mn2 (at 170 K) at Mn4 (at 150 K) upon heating and cooling reveal no thermal historical effects, as shown in Fig. S3.

The temperature dependence of the lattice parameters in Mn-doped (Hf, Ta)Fe_2 is examined to assess their potential for thermal expansion applications. As shown in Fig. 8, the lattice parameters were derived from NPD patterns at various temperatures. The lattice parameter *c* increases normally with rising tempera-

Table 3
Fitted NPD parameters for the Mn0, Mn2, and Mn4 alloys obtained at different temperatures. The lattice structure corresponds to the hexagonal $P6_3/mmc$ symmetry (space group 194) with Fe atoms occupying the 2*a* site at position (0,0,0) and the 6*h* site at position (x, $2x$, 1/4) while Hf/Ta atoms are located at the 4*f* site with position (1/3, 2/3, z).

sample	T (K)	$x_{(6h)}$	$z_{(4f)}$	c/a	$M_{Fe(6h)}$ (μ_B/f.u.)	$M_{Fe(2a)}$ (μ_B/f.u.)	R_{wp} (%)
Mn0	400	0.16904(23)	0.56328(15)	1.63418(5)	–	–	4.43
	300	0.16897(14)	0.56314(29)	1.63546(6)	–	–	5.05
	4	0.16889(21)	0.56269(15)	1.62987(4)	1.47	1.36	5.33
Mn2	400	0.16947(26)	0.56326(18)	1.63394(6)	–	–	4.77
	300	0.16902(27)	0.56326(18)	1.63544(6)	–	–	5.01
	170	0.16890(25)	0.56255(18)	1.63116(6)	1.01	0.84	5.76
	4	0.16925(24)	0.56256(16)	1.62993(5)	1.25	1.2	5.71
Mn4	400	0.16951(28)	0.56322(20)	1.63403(7)	–	–	4.91
	300	0.16935(16)	0.56308(33)	1.63514(7)	–	–	5.18
	150	0.16917(29)	0.56311(11)	1.63084(7)	1.06	0.84	6.29
	4	0.16903(29)	0.56216(19)	1.62996(6)	1.4	0.96	6.41

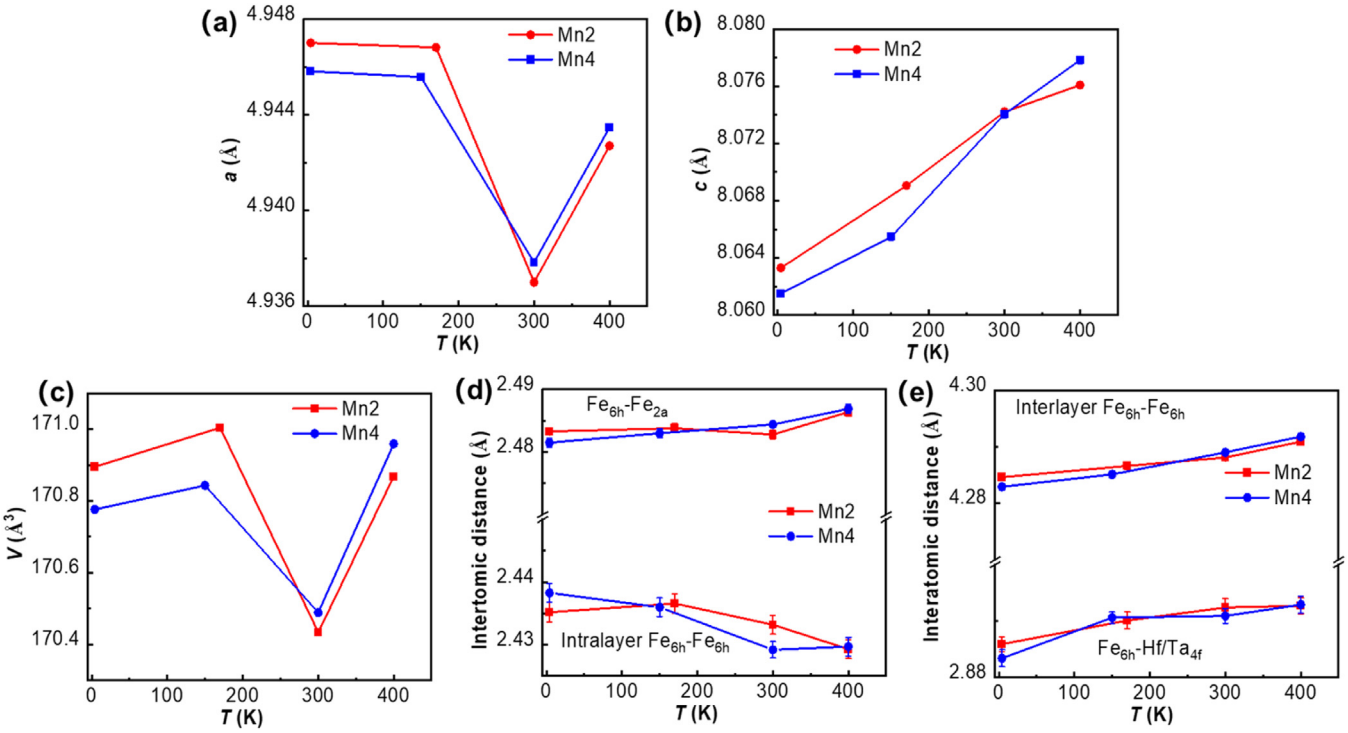

Fig. 8. Temperature dependence of (a, b) lattice parameter *a, c* and (c) unit-cell volume *V* derived from NPD patterns. (d, e) Interatomic distances as a function of temperature, illustrating changes in the Fe-Fe and Fe-Hf/Ta distances across different temperature ranges.

ture, while the unit-cell volume *V* shows a typical positive thermal expansion from 4 K up to 150–170 K, above which a contraction begins, indicating negative thermal expansion behavior, associated with the FM-AFM transition. At room temperature, the *V* of the Mn4 alloy is larger than that of the Mn2 alloy, consistent with the XRD result. However, at 4 K, the unit-cell volume *V* of the Mn4 alloy is smaller than that of the Mn2 alloy. The small variation in volume or lattice parameter *a* prior to AFM-FM transition responds to the collapse of magnetic moment oriented within the *a*–*b* plane [33]. These results indicate that Mn doping in (Hf,Ta)Fe_2 alloys could be a potential strategy to tune thermal expansion in Fe-based Laves phase. Fig. 8(d, e) shows the interatomic distance of Fe atoms derived from NPD patterns. The interlayer distances, including Fe_{6h}-Fe_{6h}, Fe_{6h}-Fe_{2a}, and Fe_{6h}-Hf/Ta_{4f}, increases linearly with temperature. In contrast, a decrease in the Fe_{6h}-Fe_{6h} intralayer spacing is observed between 150/170 K and 300 K. Similar trends have been reported for the temperature-dependence of magnetism in $Fe_2Sc_{0.4}Ti_{0.6}$ [58] and $Fe_2Hf_{0.85}Ti_{0.15}$ [59]. The small variation of lattice parameters prior to AFM-FM transition in the Mn4 alloy may be linked to the reduction in the shortest Fe_{6h}-Fe_{6h} distance between 4 and 150 K. This shortest Fe_{6h}-Fe_{6h} distance is critical in controlling the magnetic interactions in Fe-based Laves phases [59].

To further understand the influence of Mn substitution and Fe vacancies on the magnetic and structural stability of the (Hf,Ta)Fe_2 system, we employed spin-polarized DFT calculations to examine formation energy, lattice parameters, and magnetic moment in the $Hf_{0.80}Ta_{0.20}Fe_{2-x}$ system. The calculated unit-cell volume for the Mn-doped alloy (159.58 Å) is larger than that of $Hf_{0.80}Ta_{0.20}Fe_2$ (159.42 Å) and the Fe-deficient alloy (158.52 Å), consistent with trends observed in XRD results. Comparison of the formation energies indicates that both Fe vacancies and Mn atoms preferentially occupy the 6*h* site, as shown in Fig. 9(a). As illustrated in Fig. 9(b, c), the materials exhibit metallic characteristics in the FM state, with electronic states present at the Fermi level (E_{Fermi}). Spin splitting is evident between the majority and minority spin channels in the total density of states (TDOS), resulting from exchange splitting. The TDOS yields net saturation mag-

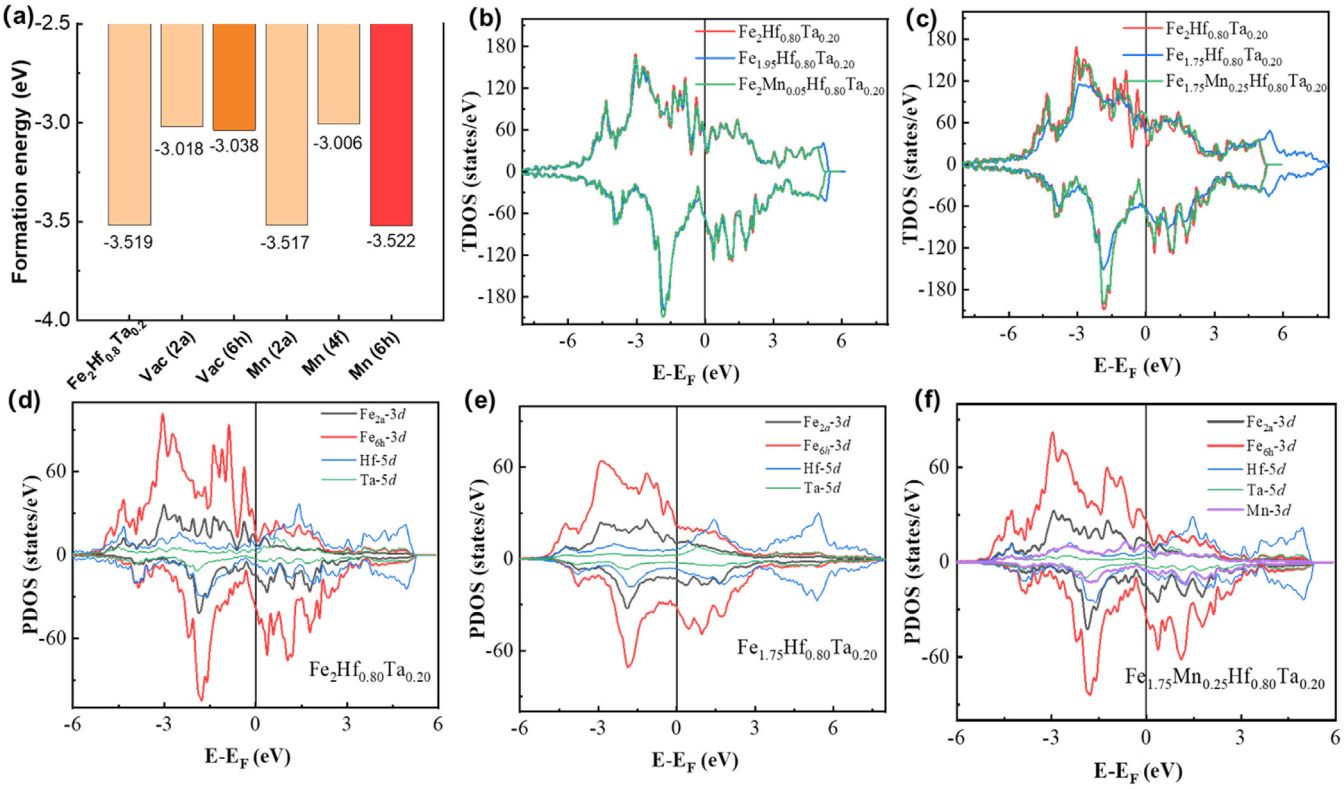

Fig. 9. (a) Formation energy E_F for different site occupations of Fe vacancies (Vac) and Mn substitutions; A low E_F indicates the preferred site. (b, c) Total density of state (TDOS) for the parent alloy, Fe-deficient system, and Mn-doped system in the FM state. (d–f) Orbital projected density of states (PDOS) for the three alloys, showing contributions from individual atomic orbitals.

netization values of 3.17 μ_B/f.u. for $Hf_{0.80}Ta_{0.20}Fe_2$, 3.06 μ_B/f.u. for $Hf_{0.80}Ta_{0.20}Fe_{1.95}$ ($Hf_{0.80}Ta_{0.20}Fe_{1.75}$, 2.77 μ_B/f.u.), and 3.12 μ_B/f.u. for $Hf_{0.80}Ta_{0.20}Fe_{1.95}Mn_{0.05}$ ($Hf_{0.80}Ta_{0.20}Fe_{1.75}Mn_{0.25}$, 2.95 μ_B/f.u.), indicating lower magnetization in the Fe-deficient alloy, which aligns with *M-H* curves observations. The PDOS shape of Fe_{6h}-3*d* and Hf-5*d* for $Hf_{0.80}Ta_{0.20}Fe_{1.75}$ shows obvious differences compared to $Hf_{0.80}Ta_{0.20}Fe_2$ and $Hf_{0.80}Ta_{0.20}Fe_{1.75}Mn_{0.25}$ as shown in Fig. 9(e), which accounts for the smallest calculated magnetization in $Hf_{0.80}Ta_{0.20}Fe_{1.75}$. Below E_{Fermi}, the overlap of Fe-3*d* and Hf/Ta-5*d* peaks around −1.6 eV indicates typical *d–d* hybridization, with *d* electrons to Hf/Ta atoms [57,60,61]. The magnetic moment of the Mn atom (1.26 μ_B) in $Hf_{0.80}Ta_{0.20}Fe_{1.95}Mn_{0.05}$ and $Hf_{0.80}Ta_{0.20}Fe_{1.75}Mn_{0.25}$ is lower than that of the Fe atoms (1.47 μ_B at 2*a* and 1.61μ_B at 6 h for the former and 1.33 μ_B at 2*a* and 1.53 μ_B at 6*h* for the latter). The magnetic moments derived from Neutron diffraction, Mössbauer spectroscopy, and DFT calculations, as shown in Table S2, exhibit good consistency. The limited hybridization between Mn(3*d*) and Fe(3*d*), along with the low Mn content, leads to the minimal difference in magnetization between the minor Mn-doped and parent alloys, ascribing to the tunable magnetoelastic transition [57,58,62]. The magnetic moments of Fe at the 2*a* site are frustrated in the AFM state, positioned between two antiferromagnetic coupled planes as identified by NPD analysis [29]. The sharp FM-AFM transition is attributed to the synchronized evolution of Fe at the 6*h* and 2*a* sites, as shown through electron spin resonance studies [16]. When the electronic state at the 6*h* site undergoes slight changes due to Mn substitution or Fe vacancies, the moment at the 2*a* site becomes unsynchronized, causing a shift in the magnetoelastic transition temperature. Consequently, Mn substitution and Fe off-stoichiometry result in a broadened magnetoelastic transition temperature window in $Hf_{0.82}Ta_{0.18}Fe_2$-based alloys. Although further broadening of the transition temperature is somewhat suppressed by the inhomogeneous distribution of Mn atoms in high-Mn alloy, the abilities to specifically control the specific Fe sites offers a pathway to further optimize the magnetocaloric response in (Hf,Ta) Fe_2 Laves phase alloys.

5. Conclusions

This study investigated the impacts of Fe off-stoichiometry and Mn substitution on the structural, magnetic, and thermal properties of $Hf_{0.82}Ta_{0.18}Fe_2$-based Laves phase. All samples crystallize in a single-phase hexagonal *C*14-type structure, with Mn atoms and Fe vacancies preferentially occupying the 6*h* site, confirmed by DFT calculations and NPD analysis. Mn substitution led to an increase in unit-cell volume due to Mn's larger atomic radius, while Fe vacancies induced lattice contraction, creating a tunable structure that influences magnetic and thermal behaviors. The small variation in volume or lattice parameter *a* prior to AFM-FM transition responds to the collapse of the magnetic moment oriented within the *a–b* plane. Notably, a table-like entropy change of 1.7–2.2 J/(kg K) for a magnetic field change of 2 T was achieved over a wide temperature range of 190–260 K by adjusting the Mn and Fe contents. Mössbauer spectroscopy and DFT calculations revealed that Mn substitution slightly affects the magnetic interactions and alters the electronic state of Fe at the 6*h* site, contributing to the modification of the frustration effect of (Hf,Ta)Fe_2 alloys. These findings provide valuable insights into the role of magnetic atoms in the magnetoelastic transition in Fe-based Laves phase alloys, and the site-specific control offers a pathway for optimizing the magnetocaloric properties of Fe-based Laves phase alloys and inspires the design of other promising MCE materials with magnetoelastic transitions.

Declaration of competing interest

The authors declare that they have no known competing financial interests or personal relationships that could have appeared to influence the work reported in this paper.

CRediT authorship contribution statement

Qi Shen: Writing – original draft, Project administration, Funding acquisition, Formal analysis. **Floris van Rooij:** Methodology, Investigation, Formal analysis, Data curation. **Zeyu Zhang:** Formal analysis, Data curation. **Weixiang Hao:** Software. **Achim Iulian Dugulan:** Resources. **Niels van Dijk:** Writing – review & editing, Supervision. **Ekkes Brück:** Writing – review & editing, Supervision, Funding acquisition. **Lingwei Li:** Writing – review & editing, Funding acquisition.

Acknowledgements

This work was financially supported by the Dutch Research Council (No. 680-91-013) and the National Natural Science Foundation of China (Nos. 52401230 and 52472274). The authors thank Anton Lefering, Bert Zwart, and Robert Dankelman (PEARL NPD) for their technical assistance and acknowledge the Supercomputing Center of Hangzhou Dianzi University for providing computing resources.

Supplementary materials

Supplementary material associated with this article can be found, in the online version, at doi:10.1016/j.jmst.2025.08.015.

References

[1] O. Tegus, E. Brück, K.H.J. Buschow, F.R. de Boer, Nature 415 (2002) 150–151.
[2] J. Liu, T. Gottschall, K.P. Skokov, J.D. Moore, O. Gutfleisch, Nat. Mater. 11 (2012) 620–626.
[3] O. Gutfleisch, M.A. Willard, E. Bruck, C.H. Chen, S.G. Sankar, J.P. Liu, Adv. Mater. 23 (2011) 821–842.
[4] Y. Zhang, A. Li, W. Hao, H.F. Li, L. Li, Acta Mater. 292 (2025) 121033.
[5] F. Zhang, X. Miao, N. van Dijk, E. Brück, Y. Ren, Adv. Energy Mater. 14 (2024) 2400369.
[6] Y.K. Zhang, Y. Na, X. Zhao, Y. Xie, J. Mater. Chem. A (2025) 19923–19932.
[7] J.V.K. Pecharsky, K.A. Gschneidner, Phys. Rev. Lett. 78 (1997) 4494–4497.
[8] A. Chirkova, K.P. Skokov, L. Schultz, N.V. Baranov, O. Gutfleisch, T.G. Woodcock, Acta Mater. 106 (2016) 15–21.
[9] A. Fujita, S. Fujieda, Y. Hasegawa, K. Fukamichi, Phys. Rev. B 67 (2003) 104416.
[10] L. Miao, X. Lu, Z. Wei, Y. Zhang, Y. Zhang, J. Liu, Acta Mater. 245 (2023) 118635.
[11] N.H. Dung, Z.Q. Ou, L. Caron, L. Zhang, D.T.C. Thanh, G.A. de Wijs, R.A. de Groot, K.H.J. Buschow, E. Brück, Adv. Energy Mater. 1 (2011) 1215–1219.
[12] L. Caron, X.F. Miao, J.C.P. Klaasse, S. Gama, E. Brück, Appl. Phys. Lett. 103 (2013) 112404.
[13] Z. Song, Z. Li, B. Yang, H. Yan, C. Esling, X. Zhao, L. Zuo, Materials 14 (2021) 1–11.
[14] Q. Shen, F. Zhang, I. Dugulan, N. van Dijk, E. Brück, Scr. Mater. 232 (2023) 115482.
[15] A. Tekgül, M. Acet, F. Scheibel, M. Farle, N. Ünal, Acta Mater. 124 (2017) 93–99.
[16] L.F. Li, P. Tong, Y.M. Zou, W. Tong, W.B. Jiang, Y. Jiang, X.K. Zhang, J.C. Lin, M. Wang, C. Yang, X.B. Zhu, W.H. Song, Y.P. Sun, Acta Mater. 161 (2018) 258–265.
[17] T.H.Y. Nagata, S. Yashiro, H. Samata, S. Abe, J. Alloys Compd. 292 (1999) 11–20.
[18] B. Li, X.H. Luo, H. Wang, W.J. Ren, S. Yano, C.W. Wang, J.S. Gardner, K.D. Liss, P. Miao, S.H. Lee, T. Kamiyama, R.Q. Wu, Y. Kawakita, Z.D. Zhang, Phys. Rev. B 93 (2016) 224405.
[19] M. Polanski, M. Kwiatkowska, I. Kunce, J. Bystrzycki, Int. J. Hydrog. Energy 38 (2013) 12159–12171.
[20] C. Qin, C. Zhou, L. Ouyang, J. Liu, M. Zhu, T. Sun, H. Wang, Int. J. Hydrog. Energy 45 (2020) 9836–9844.
[21] K. Inoue, K. Tachikawa, Appl. Phys. Lett. 25 (1974) 94–96.
[22] Y. Hishinuma, A. Kikuchi, Y. Iijima, Y. Yoshida, T. Takeuchi, A. Nishimura, K. Inoue, J. Nucl. Mater. 329-333 (2004) 1580–1584.
[23] A.E. Clark, H.S. Belson, Phys. Rev. B 5 (1972) 3642–3644.
[24] Z. Zhou, J. Li, X. Bao, Y. Zhou, X. Gao, J. Alloys Compd. 826 (2020) 153959.
[25] L.V.B. Diop, O. Isnard, M. Amara, F. Gay, J.P. Itié, J. Alloys Compd. 845 (2020) 156310.
[26] L.V.B. Diop, J. Kastil, O. Isnard, Z. Arnold, J. Kamarad, J. Alloys Compd. 627 (2015) 446–450.
[27] H.G.M. Duijn, E. Brück, A.A. Menovsky, K.H.J. Buschow, F.R. de Boer, R. Coehoorn, M. Winkelmann, K. Siemensmeyer, J. Appl. Phys. 81 (1997) 4218–4220.
[28] H.R. Rechenberg, L. Morellon, P.A. Algarabel, M.R. Ibarra, Phys. Rev. B 71 (2005) 104412.
[29] L.V.B. Diop, O. Isnard, E. Suard, D. Benea, Solid State Commun. 229 (2016) 16–21.
[30] L. Li, P. Tong, W. Tong, W. Jiang, Y. Ding, H. Lin, J. Lin, C. Yang, F. Zhu, X. Zhang, X. Zhu, W. Song, Y. Sun, Inorg. Chem. 58 (2019) 16818–16822.
[31] D. Cen, B. Wang, R. Chu, Y. Gong, G. Xu, F. Chen, F. Xu, Scr. Mater. 186 (2020) 331–335.
[32] J.F. Herbst, C.D. Fuerst, R.D. McMichael, J. Appl. Phys. 79 (1996) 5998.
[33] J. Xu, Z. Wang, H. Huang, Z. Li, X. Chi, D. Wang, J. Zhang, X. Zheng, J. Shen, W. Zhou, Y. Gao, J. Cai, T. Zhao, S. Wang, Y. Zhang, B. Shen, Adv. Mater. 35 (2023) 2208635.
[34] J. Dong, M. Zhang, J. Liu, P. Zhang, A. Yan, Physica B 476 (2015) 171–174.
[35] B.H. Toby, Powder Diffr. 21 (2012) 67–70.
[36] Z. Klencsar, Nucl. Instrum. Meth. B 129 (1997) 527–533.
[37] L. van Eijck, L.D. Cussen, G.J. Sykora, E.M. Schooneveld, N.J. Rhodes, A.A. van Well, C. Pappas, J. Appl. Crystallogr. 49 (2016) 1398–1401.
[38] T.M. Sabine, J. Appl. Cryst. 10 (1977) 277–280.
[39] J. Rodriguez-Carvajal, Physica B 192 (1993) 55–69.
[40] G. Kresse, J. Hafner, Phys. Rev. B-Condens. Matter. 47 (1993) 558–561.
[41] G. Kresse, J. Furthmuller, Comput. Mater. Sci. 6 (1996) 15–50.
[42] P.E. Blochl, Phys. Rev. B-Condens. Matter. 50 (1994) 17953–17979.
[43] G. Kresse, D. Joubert, Phys. Rev. B 59 (1999) 1758–1775.
[44] J.P. Perdew, K. Burke, M. Ernzerhof, Phys. Rev. Lett. 77 (1996) 3865–3868.
[45] N.N. Greenwood, A. Earnshaw, Chemistry of the Elements, 2nd ed., Butterworth-Heinemann, Oxford, 1997.
[46] Q. Shen, Z. Zhang, C. de Vries, A.I. Dugulan, N. van Dijk, E. Brück, L. Li, Chem. Mater. 36 (2024) 6299–6305.
[47] H. Zhong, Y. Song, F. Long, H. Lu, M. Ai, T. Li, Y. Yao, Y. Sakai, M. Ikeda, K. Takahashi, M. Azuma, F. Hu, X. Xing, J. Chen, Adv. Mater. 36 (2024) 2402046.
[48] Y. Huang, Z. Han, Z. Jiang, S. Li, Y. Hsia, Physica B 388 (2007) 354–358.
[49] H. Wang, Y.H. Wang, Y.Y. Gong, G.Z. Xu, E. Liu, X.F. Miao, Y.J. Zhang, Y.Y. Shao, J. Liu, N. Ui Hassan, I.A. Shah, F. Xu, Rare Metals 43 (2024) 6596–6605.
[50] L. Sun, H. Yibole, O. Tegus, F. Guillou, Crystals 10 (2020) 410.
[51] Y. Nishihara, J. Phys. Soc. Jpn. 52 (1983) 3630–3636.
[52] A.M. Aliev, A.B. Batdalov, L.N. Khanov, A.P. Kamantsev, V.V. Koledov, A.V. Mashirov, V.G. Shavrov, R.M. Grechishkin, A.R. Kaul, V. Sampath, Appl. Phys. Lett. 109 (2016) 202407.
[53] K.G. Sandeman, Scr. Mater. 67 (2012) 566–571.
[54] N.N. Delyagin, A.L. Erzinkyan, V.P. Parfenova, I.N. Rozantsev, G.K. Ryasny, J. Magn. Magn. Mater. 320 (2008) 1853–1857.
[55] Y.J. Huang, S.Z. Li, Z.D. Han, W.X. Wang, Z.Y. Jiang, S.L. Huang, J. Lin, Y.F. Hsia, J. Alloys Compd. 427 (2007) 37–41.
[56] O. Eriksson, A. Svanet, J. Phys-Condens. Mater. l (1989) 1589–1599.
[57] F. Zhang, P. Feng, A. Kiecana, Z. Wu, Z. Bai, W. Li, H. Chen, W. Yin, X.W. Yan, F. Ma, N.V. Dijk, E. Brück, Y. Ren, Adv. Funct. Mater. 34 (2024) 2409270.
[58] Y. Song, Q. Sun, M. Xu, J. Zhang, Y. Hao, Y. Qiao, S. Zhang, Q. Huang, X. Xing, J. Chen, Mater. Horiz. 7 (2020) 275–281.
[59] Q. Shen, I. Batashev, F. Zhang, H. Ojiyed, I. Dugulan, N. van Dijk, E. Brück, Acta Mater. 257 (2023) 119149.
[60] Y. Zhang, Y. Na, W. Hao, T. Gottschall, L. Li, Adv. Funct. Mater. (2024) 2409061.
[61] F. Chen, J. Xu, X. Zhao, Y. Na, Y. Zhang, Sci. China Mater. 68 (2025) 2828–2840.
[62] X.F. Miao, L. Caron, P. Roy, N.H. Dung, L. Zhang, W.A. Kockelmann, R.A. de Groot, N.H. van Dijk, E. Brück, Phys. Rev. B 89 (2014) 174429.